

Stabilizing simulation-based cosmological Fisher forecasts: a case study using the Voronoi volume function

Saeed Dhawalikar,^{a,1} Aseem Paranjape,^a and Shadab Alam^b

Inter-University Centre for Astronomy & Astrophysics,
Ganeshkhind, Post Bag 4, Pune 411007, India
Tata Institute of Fundamental Research, Homi Bhabha Road, Mumbai 400005, India
E-mail: saeed.dhawalikar@iucaa.in, aseem@iucaa.in, shadab.alam@tifr.res.in

Abstract. Forecasting cosmological constraints from halo-based statistics often suffers from instability in derivative estimates, especially when the number of simulations is limited. This instability reduces the reliability of Fisher forecasts and machine learning based approaches that use derivatives. We introduce a general framework that addresses this challenge by stabilizing the input statistic and then systematically identifying the optimal subset of summary statistics that maximizes cosmological information while simultaneously minimizing the instability of predicted constraints. We demonstrate this framework using the Voronoi volume function (VVF), a summary statistic that captures beyond two-point clustering information. Applying our two-step procedure – random sub-sampling followed by optimization – improves the constraining power by up to a factor of 2, while also enhancing the stability of the forecasts across realizations. As surveys like Euclid, DESI, and LSST push toward tighter constraints, the ability to produce stable and accurate theoretical predictions is essential. Our results suggest that new summary statistics such as the VVF, combined with careful data curation and stabilization strategies, can play a key role in next-generation precision cosmology.

Keywords: Statistical sampling techniques, cosmological parameters from LSS, cosmological simulations

¹Corresponding author.

Contents

1	Introduction	1
2	Numerical Techniques	2
2.1	N-body simulations	2
2.2	Halo samples	3
2.3	Voronoi volume function	4
3	Statistical techniques	5
3.1	Multiple simulation realizations	7
3.2	Single Simulation realization	9
4	Results	10
4.1	Multiple simulation realizations	10
4.2	Single simulation realization	12
5	Discussion	15
A	Covariance and Fisher matrices	20
B	Random sub-sampled vs Full VVF	21
C	Choice of parameter variations	22

1 Introduction

The Large-Scale Structure (LSS) of the Universe contains a wealth of information about the underlying cosmological model (including the nature of dark matter, dark energy and initial conditions) as well as the physics of galaxy formation and evolution. With the increasing volume, depth, and precision of ongoing and upcoming LSS surveys such as the Dark Energy Spectroscopic Instrument (DESI) [1, 2], Rubin-LSST [3] and Euclid [4], it is now possible to probe the matter distribution of the Universe with unprecedented detail. These surveys will unlock immense information; at the same time they present a significant analysis challenge: identifying summary statistics that are both robust and maximally informative for constraining cosmological parameters.

Traditionally, analyses of the LSS have relied on two-point statistics like the two-point correlation function (2PCF) and the power spectrum, which would represent complete summaries if cosmic structure were Gaussian distributed. However, as structure formation becomes increasingly nonlinear at late times, a significant fraction of the cosmological information resides in higher-order correlations that are not captured by these conventional methods. This motivates the exploration of alternative and complementary summary statistics that can probe non-Gaussian features and environmental dependence more effectively.

In recent years, a wide range of non-Gaussian, halo-based statistics have been developed to capture such higher-order information. These include, but are not limited to, the k-nearest-neighbor (kNN) distribution [5, 6], marked correlation functions [7, 8] and Minkowski

functionals [9, 10]. Each of these probes the LSS in a unique way, targeting higher-order spatial correlations. In addition, simulation-based inference (SBI) methods that utilize machine learning have emerged, which employ neural networks to learn compact summary statistics directly from simulations [11–15]. The Voronoi volume function (VVF), introduced in [16] and used below, is another recent promising summary statistic, that accesses the beyond-Gaussian information through the distribution of cell volumes in the Voronoi tessellation of the given set of tracers. As demonstrated in recent studies [16, 17], VVF captures higher-order clustering and assembly bias signatures, and potentially provides cosmological constraints that are complementary to those from the 2PCF.

Despite the potential of these advanced halo-based statistics, their use in Fisher forecasts and cosmological inference faces practical challenges. The estimation of robust covariance matrices and stable numerical derivatives of these statistics with respect to cosmological parameters – which is typically done via finite differences using simulation suites – requires a large number of simulation realizations. For instance, robust Fisher analyses and simulation-based inference applications often allocate $\mathcal{O}(100)$ realizations specifically for derivative estimation [18–21]. This is not always feasible, especially in case of high-resolution large-volume simulations. Without careful treatment, this limitation leads to noisy derivatives and unreliable Fisher estimates. The need for a robust, reproducible and computationally efficient method to extract information from such halo-based statistics is therefore imminent.

In this paper, we present a general formalism that reduces the noise in the choice of summary statistic by averaging over multiple random sub-samples, and then identifies a subset of data points that maximizes the stability and information content in the Fisher forecast. Our method is agnostic to the specific choice of statistic, and relies on a general method to stabilize the statistic of interest using random sub-sampling and simple diagnostics to quantify the informativeness, accuracy and stability of derivatives with respect to the cosmological parameters to be constrained, without invoking expensive machine learning techniques. While the VVF serves as a case study in this paper, our method is general and applicable to any halo-based, field-based or neural summary statistic involving noisy derivative estimates. As we enter an era of precision cosmology driven by increasingly complex datasets, such methods will be essential to extract reliable constraints from the nonlinear Universe.

The paper is organized as follows. Section 2 describes the suite of N-body simulations used in this work, along with the tracer sample selection. It also provides a brief overview of the VVF and outlines how it is used for Fisher forecasting. In Section 3, we present our formalism for selecting an optimal subset of data points for Fisher analysis in two scenarios: (a) when multiple realizations are available to estimate the covariance matrix, along with a few seed-matched cosmological variations of the simulations; and (b) when only a single realization per cosmology is available, with jackknife resampling used to estimate the covariance. In Section 4, we apply this method to the VVF measured from two tracer samples and demonstrate its effectiveness, and conclude in Section 5.

2 Numerical Techniques

2.1 N-body simulations

We use a suite of N-body simulations named *Sinhagad* to perform a Fisher forecast analysis based on the VVF. The default simulations adopt cosmological parameters consistent with the Planck 2018 results [22]. For the Fisher analysis, each of the six cosmological parameters is

Parameter	Default value (θ_0)	Variation magnitude Δ
Ω_m	0.3138	0.05 Ω_{m0}
n_s	0.9649	0.05 n_{s0}
h	0.6736	0.05 h_0
A_s	2.0989×10^{-9}	0.1 A_{s0}
Ω_b	0.0493	0.1 Ω_{b0}
Ω_k	0.0	0.05

Table 1: Cosmological parameters and variations of the **Sinhagad** simulation suite.

Variation	Variation magnitude	Realizations
Default	-	101
Ω_m	$\pm 2\Delta, \pm\Delta, \pm\Delta/2$	3
n_s	$\pm 2\Delta, \pm\Delta, \pm\Delta/2$	3
h	$\pm 2\Delta, \pm\Delta$	1
A_s	$\pm 2\Delta, \pm\Delta$	1
Ω_b	$\pm 2\Delta, \pm\Delta$	1
Ω_k	$\pm 2\Delta, \pm\Delta$	1

Table 2: Summary of number of simulations in the **Sinhagad** simulation suite for each cosmological parameter variation.

varied individually while keeping the others fixed. Table 1 summarizes the default parameter values (θ_0) along with their respective variations (Δ).

All simulations have a periodic comoving box of size $L_{\text{box}} = 200 h^{-1} \text{Mpc}$ and 256^3 particles, corresponding to a particle mass of $4.15 \times 10^{10} h^{-1} M_\odot$. For each cosmological parameter, 4 simulations are performed, with the parameters taking values $\theta_0 \pm 2\Delta, \theta_0 \pm \Delta$. These variation simulations are seed matched with one of the default realizations, namely $r1$. Additionally, two more sets of seed matched simulation variations are performed for Ω_m, n_s , along with variations of $\pm\Delta/2$. These two parameters are the primary focus of this paper. For the estimation of the covariance matrices, 100 additional realizations of the default simulation are used. A summary of all simulations in the **Sinhagad** suite is provided in Table 2.

The simulations are performed using the tree-PM code GADGET-4[23], with a comoving force softening length set to $1/30$ of the mean inter-particle spacing, and a PM grid of 512^3 . Initial conditions are generated at redshift $z = 49$ using second-order Lagrangian Perturbation Theory [24], implemented via N-GENIC, which is integrated into GADGET-4. A total of 201 snapshots are saved between $z = 12$ and $z = 0$, evenly spaced in scale factor $a \equiv (1+z)^{-1}$. All the analysis in this work, however, is performed using the snapshot at $z = 0$ in each simulation.

2.2 Halo samples

Dark matter halos in the simulations are identified using the six-dimensional phase-space Friends-of-Friends algorithm implemented in ROCKSTAR [25], and halo merger trees are constructed with the CONSISTENT-TREES code [26]. Halo samples are selected based on a threshold in their maximum circular velocity along the main progenitor branch in the merger tree, denoted as V_{peak} . This quantity is chosen because it closely correlates with the stellar mass

of the associated galaxy in subhalo abundance matching (see, e.g., [27–29]). Only halos resolved with at least 40 particles are considered, with halo mass defined as m_{200b} . Here, m_{200b} refers to the gravitationally bound mass within a radius R_{200b} , which encloses a region with density 200 times the mean matter density of the Universe. Additionally, halos are cleaned based on the degree of relaxation – $\eta \equiv 2T/|U|$, where T and U denote the total kinetic and gravitational potential energy of the halo, respectively. Following [30], only halos with $0.5 \leq \eta \leq 1.5$ are retained. The selection thresholds are chosen to maintain a fixed number density of tracers across all simulations for each sample.

Choosing a very high number density introduces sample incompleteness, as a larger fraction of halos fall below the resolution threshold of 40 particles when selecting by V_{peak} . To minimize this, we choose the number density such that, before enforcing the 40 particle cut, the fraction of unresolved halos in the sample selected by the corresponding V_{peak} cut is $\leq 1\%$ of the total sample. Conversely, very low number densities lead to increased noise in both the VVF measurement (see section 2.3 for details) and the corresponding covariance matrix estimates. Balancing these considerations, two tracer samples are selected with comoving number densities of $n = 2.0 \times 10^{-4}$ and $0.7 \times 10^{-4} (h^{-1}\text{Mpc})^{-3}$.

The **Sinhagad** simulation suite serves as a pilot study for a forthcoming higher-resolution suite, **Sahyadri** (Dhawalikar *et al.*, in progress). The **Sahyadri** simulations will share the same default cosmology and box size ($L_{\text{box}} = 200, h^{-1}\text{Mpc}$), but will employ a significantly higher resolution with 2048^3 particles. For each cosmological parameter, variations of $\theta_0 \pm \Delta$ will be implemented for a single realization, seed matched to the one labeled *r1* in **Sinhagad**. Unlike **Sinhagad**, which includes 100 realizations of the default cosmology for covariance estimation, **Sahyadri** will contain only a single default realization. The formalism developed in this paper is designed to be directly applicable to the upcoming **Sahyadri** suite. All simulations and analyses used in this paper were carried out on the Pegasus cluster at IUCAA, Pune.¹

2.3 Voronoi volume function

The Voronoi volume function (VVF), introduced in [16], is defined as the cumulative distribution of cell volumes in the Voronoi tessellation [31] constructed from a set of points, such as the locations of galaxies or halos, within a given volume. Each cell represents the region closest to a particular point, with its volume inversely proportional to the local tracer number density. By capturing higher-order correlations in the spatial distribution of tracers, the VVF provides information beyond traditional two-point statistics like the two-point correlation function (2PCF). This makes it a potentially powerful probe of the non-Gaussian features of large-scale structure, which are sensitive to both cosmological parameters and galaxy formation physics.

As a relatively new statistic in cosmology, the VVF was employed alongside the 2PCF in [17] to model the redshift-space distribution of galaxies in the GAMA survey [32, 33]. This combined analysis enabled a tentative detection of assembly bias – where galaxy properties depend on environmental factors beyond the host halo mass. The VVF’s sensitivity to such higher-order environmental effects highlights its potential as a valuable tool for jointly constraining cosmology and galaxy formation models. While the primary focus of this paper is not to assess the constraining power of the VVF itself, we use it here to demonstrate the applicability of the general formalism we develop for robust and stable parameter inference.

¹<http://hpc.iucaa.in>

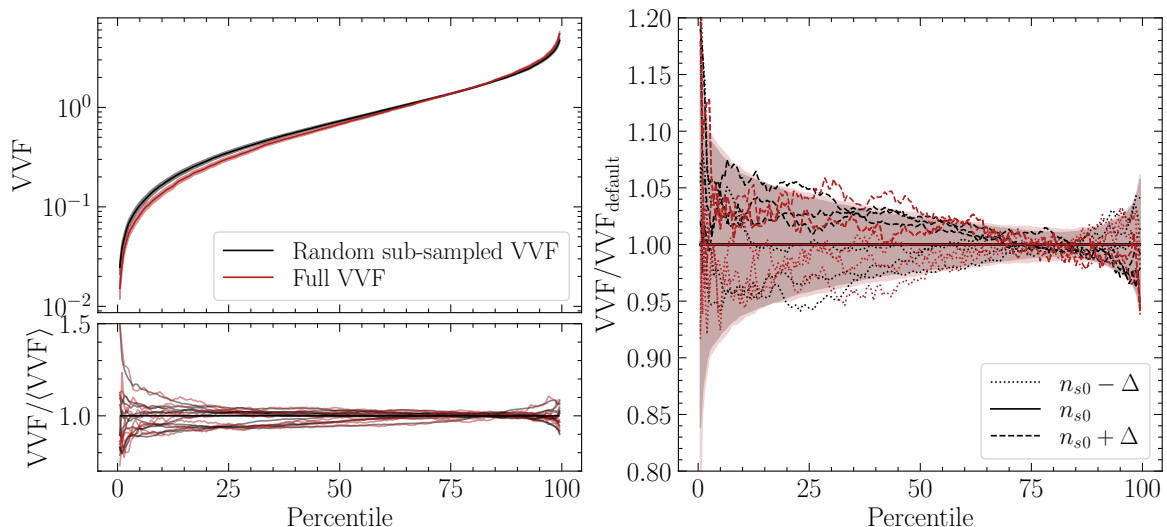


Figure 1: Illustration of VVF of the highest number density tracer sample for different simulations and choice of summary statistics. (*Top left panel*): VVF calculated using the full tracer sample in red, and the one obtained by averaging over random sub-samples in black. The solid line shows the VVF calculated for r_1 , and the bands show the diagonal errors from the covariance matrices. (*Bottom left panel*): The same two statistics scaled by the corresponding means across 100 simulation realizations, shown for 10 random realizations. It is seen that the the average statistic is less noisy. (*Right panel*): Random sub-sampled (black) and full VVF (red) for three different simulation realizations, with variations in n_s . Each curve is divided by the VVF for the default simulation of the corresponding realization. Dashed (dotted) curves show the simulations with higher (lower) n_s . Shaded regions show the diagonal errors, same as the left panel. It is seen that even after seed matching, the VVF variations are unstable especially at lower percentiles. See text for details.

The VVF is computed following the method described in [16] with an important addition: the use of random sub-sampling to suppress noise and improve stability (see Appendix B for details). For each tracer sample, 70% of the tracers are randomly selected without repetition, and the VVF is computed. This procedure is repeated 10 times, and the final VVF is obtained by averaging over these 10 realizations. Unless stated otherwise, this averaged VVF is the default statistic throughout the paper. The VVF is evaluated over percentiles ranging from 0.5 to 100, in steps of 0.5. The *left panels* in Figure 1 compare the VVF obtained using the full sample to that from the averaged sub-sample realizations. While sub-sampling naturally alters the shape of the VVF due to the reduced sampling density (see Appendix B1 of [16] for some theoretical insights), it also leads to a visibly smoother and more stable estimate, making it the preferred choice for the subsequent analysis.

3 Statistical techniques

The goal of any summary statistic is to retain maximal information about cosmological parameters in as compact a form as possible. In principle, if the data were optimally compressed – as, e.g., in the linear scheme MOPED [34] – one would only need as many summary values as there are parameters. In practice, however, due to model non-linearities and/or parameter-

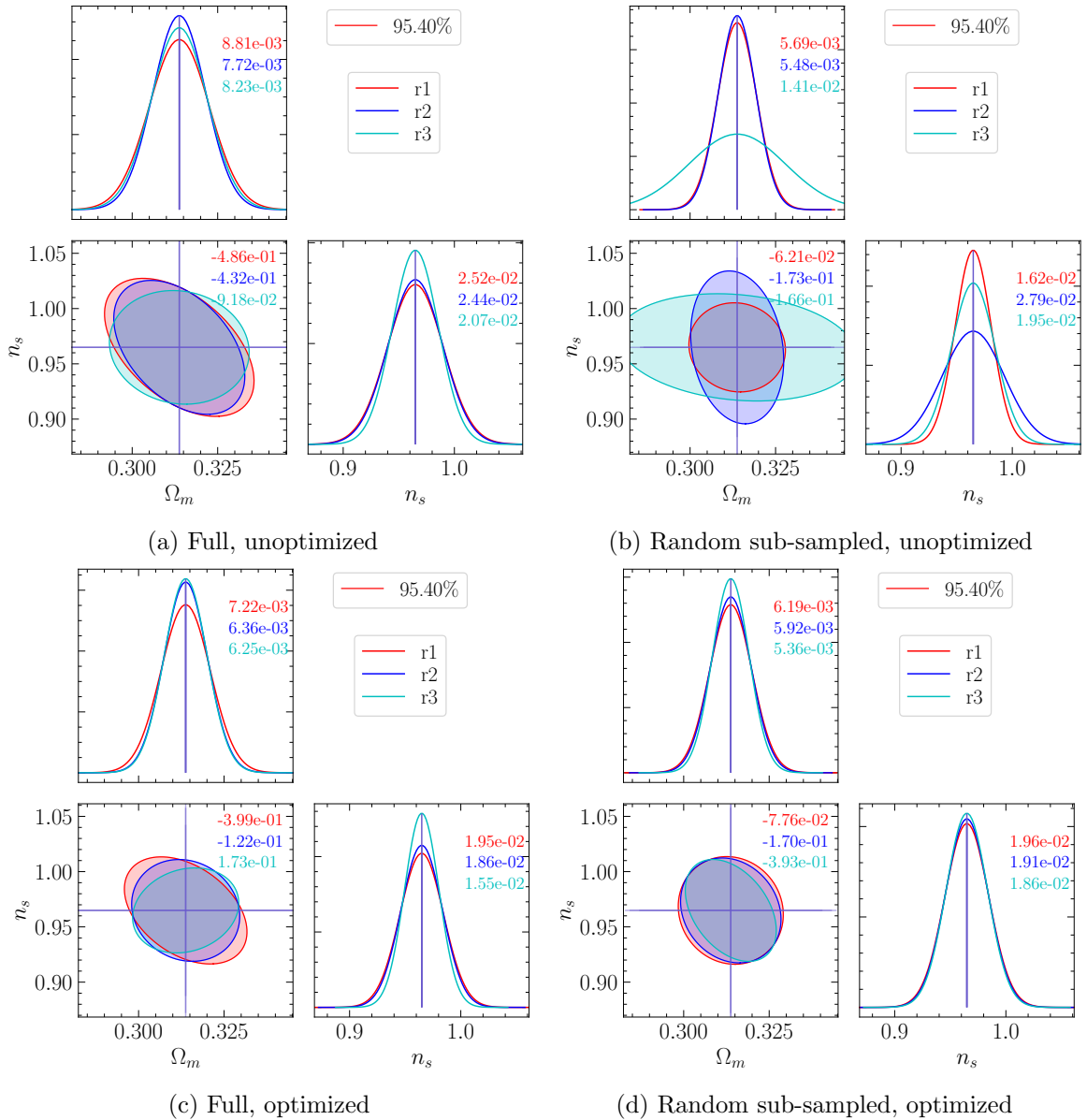


Figure 2: Corner plots from Fisher analysis performed on the highest number density tracer sample using different data selection strategies. (*Top panels*): results obtained using a data set inspired by earlier work in [16]. (*Bottom panels*): results obtained using our optimization data selection technique. *Left (right) panels* use the full (random sub-sampled) VVF for performing the Fisher analysis. It is seen random sub-sampling combined with optimization improves both the constraining power and stability of the results.

dependent covariances, one might be forced to use a larger number of summary data points. At the same time, the number of summary data points used in the Fisher forecast – denoted by N_d – must be limited. This is because estimating the covariance matrix of the statistic across realizations becomes increasingly noisy and unstable as the size of the data vector grows – unless a very large number of simulations is available. The objective, therefore, is to select an optimal subset of N_d data points from the full dataset such that the information content is maximized while ensuring that the predicted constraints remain stable across different realizations.

To illustrate the need for such optimization, the *right panel* of Figure 1 shows the VVF computed from different seed-matched simulations under small variations in the cosmological parameter n_s , using both the full tracer sample (red) and random sub-samples (black). Despite using seed-matched initial conditions, large variations persist across realizations – especially at lower percentiles. Although sub-sampling reduces some of the noise (as seen in the *left panels*), it does not eliminate the instability of the VVF’s cosmology dependence, leading to noisy and unreliable numerical derivatives. These fluctuations directly impact the accuracy and consistency of Fisher forecasts, highlighting the need for a principled method to select a subset of stable and informative statistics.

Figure 2 further illustrates the consequences of different data selection strategies on the Fisher constraints for Ω_m and n_s . The *left panels* of the Figure show the constraints obtained using the full VVF, while the *right panels* use the randomly sub-sampled version. In the *top panels*, we adopt a fixed set of 15 VVF percentiles, inspired by [17], who used the percentiles 2.5, 16, 50, 84, and 97.5. To reach a total of 15 percentiles — the maximum number for which we can robustly estimate the covariance matrix using $100 \lesssim 15^2/2$ realizations – we augment this set with additional percentiles.² We find that the constraints are quite unstable, and switching to the sub-sampled VVF does not improve this – in fact, it degrades stability in this case. Marginalized errors obtained across different seed-matched realizations can differ by up to a factor of two, even with the same choice of percentiles. In contrast, the *bottom panels* show the constraints obtained using our optimization method, which we describe in detail in the following subsections. This approach leads to noticeably tighter and more consistent constraints across different realizations. Importantly, combining the optimization with random sub-sampling yields forecasts that are both tighter and more robust, with significantly reduced sensitivity to the choice of simulation realization. This demonstrates the importance of incorporating both ingredients in Fisher analyses under limited simulation resources.

Below, we introduce an optimization framework based on three statistical measures, minimizing which allows us to quantify the balance between information gain and stability. We provide two versions of this framework: one suited for scenarios where a few seed-matched simulation sets and reliable estimates of the true parameter derivatives are available, and another applicable when such data are not accessible. The former, being more robust, is applied to the *Sinhagad* suite, while the latter, although somewhat less stringent, is suitable for use with the *Sahyadri* simulations.

3.1 Multiple simulation realizations

We consider a scenario where a sufficient number of realizations of the default simulation are available to estimate a robust covariance matrix. Additionally, accurate and noisy estimates

²The percentiles used are: 1, 2.5, 5, 7, 16, 20, 25, 50, 75, 84, 93, 95, 97.5, 98.5, 99.

of the model derivatives are available from at least two seed-matched variations. This setup corresponds to the **Sinhagad** simulation suite, which includes 100 realizations for covariance estimation, and three seed-matched sets of cosmological parameter variations for Ω_m and n_s . The accurate derivative estimates with respect to the cosmological parameters, $(dm/d\theta)_0$, for each of the 3 simulation realizations are obtained by first fitting a third order polynomial through the 7 points available at each VVF percentile from the seed-matched variation simulations, and using its first order coefficient as the estimate of the $(dm/d\theta)_0$. The noisy slope estimate, which we denote $dm/d\theta$, is obtained via a three-point central difference using the $\pm\Delta$ variations. We use the accurate and noisy estimates together to quantify the stability of numerical derivative estimates. In the ideal case, both of these will be identical.

To quantify the contribution of each data point to the Fisher information, we define:

$$Y_i \equiv \log \left(\frac{\sigma_i}{\langle (dm_i/d\theta)_{0,k} \rangle_k} \right), \quad (3.1)$$

where $\sigma_i \equiv \sqrt{C_{ii}}$ for the i -th data point or summary; the subscript k is the index of the simulation realization and the average is taken over these realizations. Smaller values of Y_i indicate that the i -th data point carries more information.

To evaluate the accuracy and stability of the derivative estimates, we define the ratio R_i^k between the noisy and accurate derivative estimates for the i -th data point in the k -th realization:

$$R_i^k \equiv \left[\frac{dm_i/d\theta}{(dm_i/d\theta)_0} \right]_k. \quad (3.2)$$

Ideally, $R_i^k = 1$. We then define two diagnostic quantities:

$$X_i \equiv \left| \log \langle R_i^k \rangle_k \right|, \quad (3.3)$$

$$Z_i \equiv \frac{\max_k(R_i^k)}{\min_k(R_i^k)}. \quad (3.4)$$

Here, X_i measures the bias of the noisy slope estimate relative to the accurate slope, while Z_i quantifies the variability of the slope across realizations. The average and the max / min of R_i^k are calculated across the realizations. A data point is retained only if $\min_k(R_i^k) \geq 0$. In this regime, the logarithm defining X_i is well defined, $X_i \geq 0$ and $Z_i \geq 1$, with $X_i = 0$ and $Z_i = 1$ corresponding to the ideal case.

To select data points that yield both stable derivatives and high information content, we impose a threshold Z_{th} and define a selection criterion in the X - Y plane. For each cosmological parameter, the valid data points are those that (i) satisfy $Z_i \leq Z_{\text{th}}$ for all parameters, and (ii) lie below the designated line in the X - Y plane. The values of Z_{th} and the line parameters are chosen empirically, and their selection is discussed in Section 4, where the procedure is applied using the VVF. Appendix B shows that using the more stable, randomly sub-sampled VVF yields a larger set of valid points, underscoring the benefit of random sub-sampling.

If the number of valid data points, N_v , exceeds the desired number N_d , a subset of size N_d must be chosen for the Fisher analysis. Assuming neighboring points are more strongly correlated — true in the case of VVF — it is advantageous to select points that are as uncorrelated as possible. While the optimal selection would ideally account for the full covariance structure, doing so is computationally expensive. As a simple proxy that

encourages de-correlation, we generate all possible equally spaced sets of N_d points from the N_v valid points and perform Fisher forecasts for each.

To evaluate the stability of the resulting forecasts, we consider the maximum value of $\max \sigma_\theta / \min \sigma_\theta$ across all θ , where σ_θ is the marginalized error on the parameter θ , and \max , \min is calculated across simulation realizations. The optimal subset of N_d points is the one that minimizes this stability metric. Although we adopt an equally spaced sampling for computational efficiency, this is not a strict requirement. In cases where correlations between neighboring points are weak, an exhaustive search over all combinations of N_d points from the N_v valid ones may be performed.

3.2 Single Simulation realization

In many cases, it is not computationally feasible to generate multiple realizations of a simulation to estimate the covariance matrix robustly. Similarly, multiple realizations of simulations with varied cosmological parameters may not be available to test the stability of the Fisher analysis. To address these limitations, we modify our formalism accordingly.

We estimate the covariance matrix using the jackknife method, and replace simulation-to-simulation variations with jackknife realizations. Furthermore, all calculations are performed assuming that only two-point parameter variations ($\pm\Delta$) are available for each cosmological parameter.

In the absence of availability of an accurately estimated slope, we modify Y by replacing the quantity $\langle (dm_i/d\theta)_0 \rangle$ with $\langle dm_i/d\theta \rangle_{\text{jk}}$, the average of the three-point finite-difference derivative computed across jackknife realizations:

$$Y_i^s \equiv \log \left(\frac{\sigma_i}{\langle dm_i/d\theta \rangle_{\text{jk}}} \right). \quad (3.5)$$

X (equation 3.3) quantifies the accuracy of the derivative in a single realization, and Z (equation 3.4) quantifies its stability across realizations. Thus, we modify these quantities to be:

$$R_{i,k}^s \equiv \frac{\max(|S_{i,k}|)}{\min(|S_{i,k}|)} \quad (3.6)$$

$$X_i^s \equiv \log \langle R_{i,k}^s \rangle_{\text{jk}}, \quad (3.7)$$

$$Z_i^s \equiv \frac{\sigma_{\text{jk}}(dm_i/d\theta)}{|\langle dm_i/d\theta \rangle_{\text{jk}}|}, \quad (3.8)$$

where the subscript jk means that the statistic of interest (such as mean or standard deviation) is calculated across the jackknife realizations, which are explicitly indexed by k when necessary. The set $S_i = \{(dm_i/d\theta)_b, (dm_i/d\theta), (dm_i/d\theta)_f\}$ includes the backward, central, and forward finite-difference slope estimates, computed using $\pm\Delta$ variations. The \max , \min in equations 3.7, 3.9 are taken over this set of 3 values for each data point indexed by i , for the k -th jackknife realization. We note that, now that 100 realizations are available, we can compute the standard deviation across these to quantify the stability across realizations using Z_i^s , whereas we were forced to use \max / \min ratio to quantify this earlier, where only 3 simulation realizations were available. This is, of course, tempered by the fact that the jackknife resampling may not capture the entirety of cosmic variance at all relevant length scales in the box.

To ensure that we only retain points whose slope estimates are consistent in sign across jackknife realizations, we define another quantity:

$$Q_i^s \equiv \left\langle \frac{\max(S_{i,k})}{\min(S_{i,k})} \right\rangle_{\text{jk}}. \quad (3.9)$$

After computing these metrics, we first discard those points with $Q_i^s \leq 0$. This is the logical equivalent of discarding points with $\min_k(R_i^k) \leq 0$ in the earlier analysis. Then, we treat X^s, Y^s, Z^s in equations (3.5)-(3.8) to be conceptually equivalent to X, Y, Z from equations (3.1)-(3.4), and follow the same procedure to identify a valid set of points based on a combination of a cut in the $X^s - Y^s$ plane, and a cut on Z^s . Note that, again, the specific choices of thresholding are application-specific. Finally, to determine the optimal subset from these valid points, we minimize the quantity:

$$q \equiv \max \left\{ \frac{\sigma_{\text{jk}}(\sigma_\theta)}{\langle \sigma_\theta \rangle_{\text{jk}}} \right\}, \quad (3.10)$$

where σ_θ is the marginalized error on parameter θ , and the maximum is taken over all cosmological parameters. This is equivalent to the last step in the earlier analysis.

4 Results

This section demonstrates the application of the formalism developed in the previous section by using the VVF to constrain two cosmological parameters: Ω_m and n_s . We focus on these two parameters as they influence the amplitude and scale dependence of clustering in the LSS, to which the VVF is expected to be sensitive. We apply the method to two different tracer samples and assess the robustness and effectiveness of the proposed optimization procedure.

In Section 4.1, we leverage the full set of simulations available in the **Sinhagad** suite to select a robust subset of VVF percentiles that yield strong and stable constraints. In Section 4.2, we test the method under limited-data conditions, emulating the setup of the **Sahyadri** suite, and evaluate the reliability of the resulting forecasts by comparing with the stable, full-simulation results.

4.1 Multiple simulation realizations

Here, we follow the procedure outlined in Section 3.1 to calculate the X, Y , and Z statistics for both cosmological parameters of interest and for the two tracer samples. Figure 3 shows scatter plots in the X - Y plane, where filled markers correspond to data points satisfying $Z \leq 3$, and open markers indicate those that do not. The threshold value $Z_{\text{th}} = 3$ is arbitrary, but we have checked that the results are not highly sensitive to small changes in this value. A very low threshold would be overly restrictive, significantly reducing the number of valid points, while a very high value compromises the stability of the constraints.

The filled markers (low- Z points) show strong clustering in the X - Y plane, and a single line in each panel can approximately separate these low- Z points from the rest. This line is common across the 4 panels, and is chosen visually to separate the strongly clustered solid points in the left bottom corner of each panel from the other scattered, mostly open points. We select only those data points that (a) lie below this line for both cosmological parameters, and (b) satisfy $Z \leq Z_{\text{th}}$, for a given number density sample.

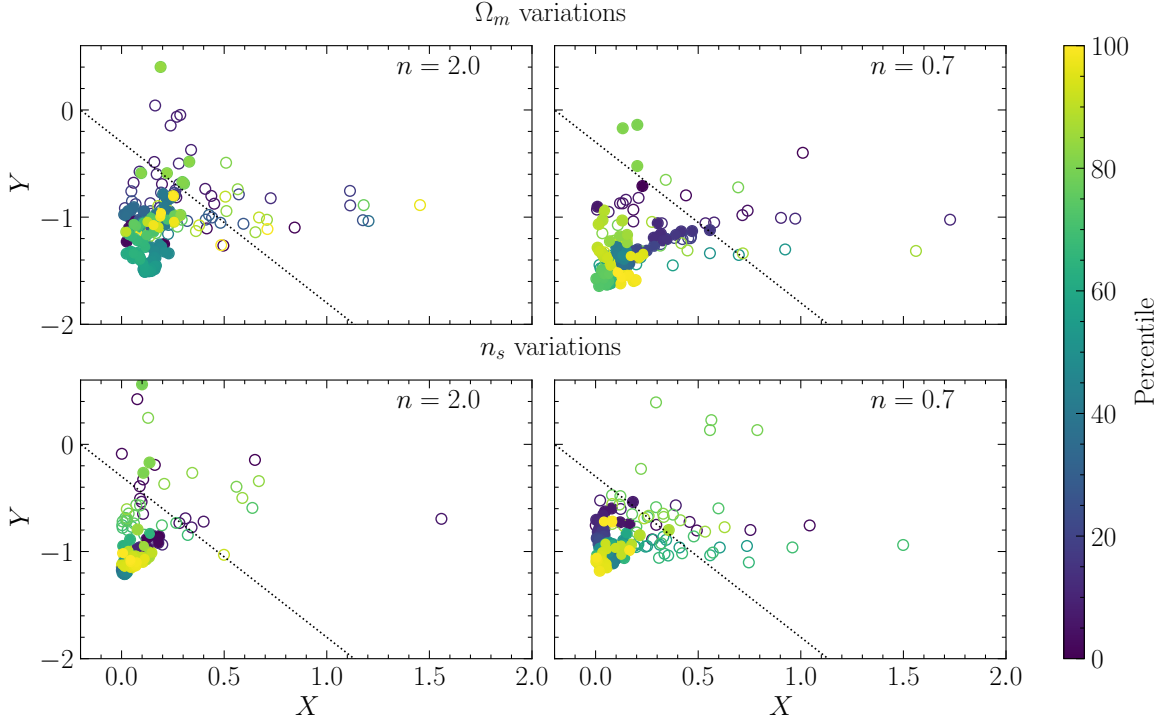


Figure 3: Scatter plots of the X and Y statistics for the two tracer samples (columns) and two cosmological parameters (rows). Each point represents a VVF data point, colour-coded by its corresponding percentile value. Filled markers indicate data points with $Z \leq 3$, while open markers correspond to points with $Z > 3$. Only points lying below the dotted lines are considered as valid data points. See Section 4.1 for further details.

Applying our optimization procedure to this filtered set, we obtain 15 selected percentiles for each tracer sample. The normalized and inverse covariance matrices corresponding to these percentiles are shown in Figure 4. We note that lower percentiles (specifically, those ≤ 32.5 and ≤ 22.5 for the higher and lower density tracer populations, respectively) are typically excluded. Additionally, there is a strong anti-correlation between the highest and lower percentiles.

Figure 5 shows the Fisher constraints obtained using the optimized percentiles for both tracer samples. The resulting forecasts are much more stable as compared to the original choice of fixed percentiles (see the *top panels* of Figure 2), with the marginalized 1D errors varying by no more than $\sim 30\%$ across simulation realizations for the lower density sample, and no more than $\sim 15\%$ for others. We also find that the VVF can constrain both Ω_m and n_s at the level of $\leq 2\%$. These constraints are upto 50% tighter as compared to the un-optimized results using the full VVF (see *top left panel* of Figure 2). However, the absolute values of constraints should not be over-interpreted: the tracer samples used here are not constructed to mimic realistic galaxy populations, and no variation in galaxy evolution physics has been included. It is also important to note that these results are based on relatively low-resolution simulations and correspondingly low number density tracer samples, in contrast to what is achievable with modern cosmological surveys. Therefore, one can expect significantly more stable constraints using higher number density samples, a possibility we will explore using

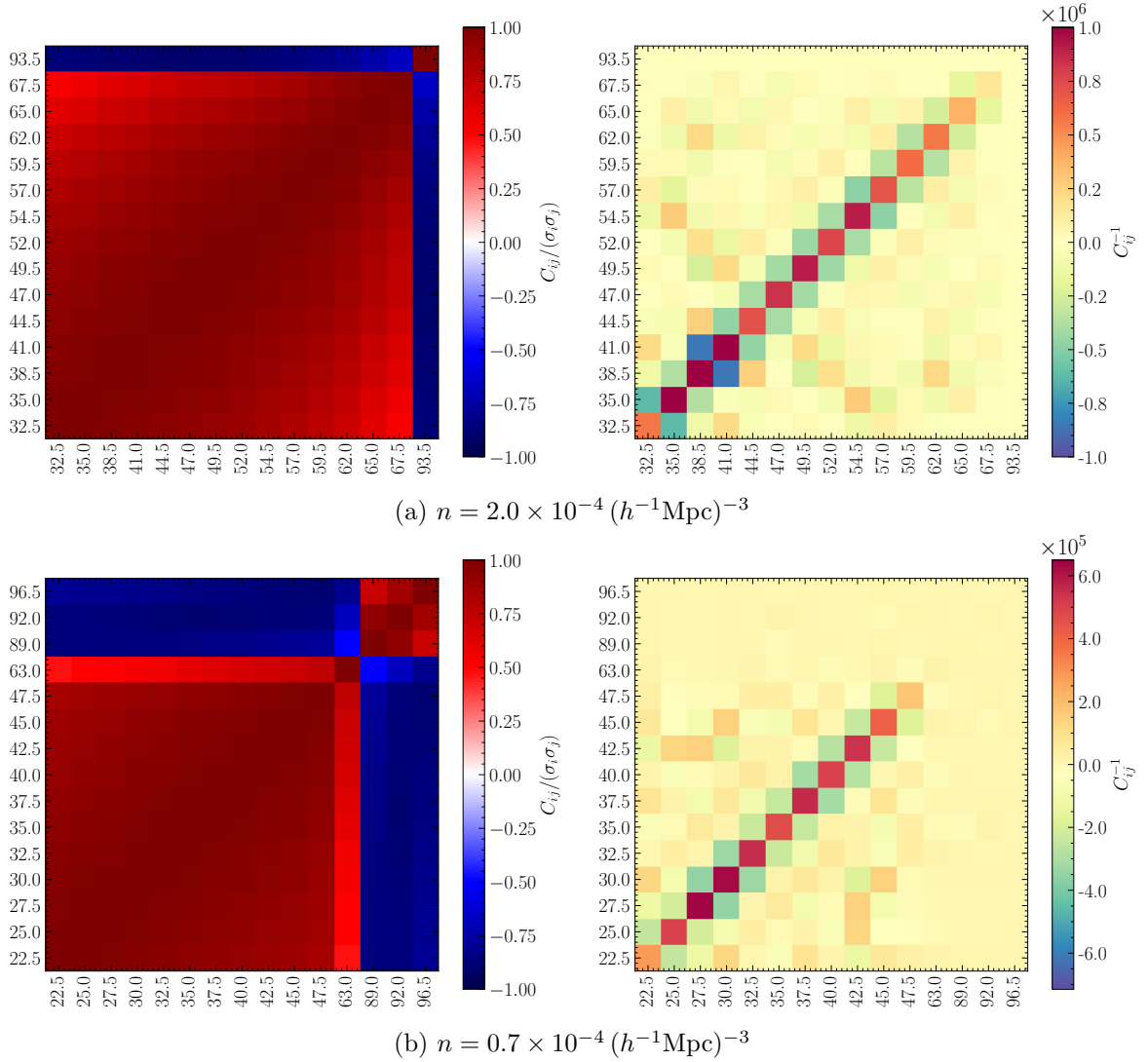


Figure 4: Normalized covariance (left) and inverse covariance matrices (right) for the two number density samples, for the optimized percentiles. It is seen that there is strong correlation between the percentiles, the higher percentiles being negatively correlated with the lower ones. These correlations are limited to only neighboring percentile bin for the inverse correlation matrices.

the **Sahyadri** suite in future work.

Finally, Figure 6 presents the Fisher constraints on all six cosmological parameters using the optimized percentiles. The two different colors represent the two tracer samples. There are interesting complementarities between the different samples, which we will explore and exploit in a more realistic analysis in future work.

4.2 Single simulation realization

We find that the covariance matrix estimated using jackknife realizations does not fully capture the true statistical uncertainties, likely due to its inability to account for cosmic variance (see Appendix A). To partially correct for this, we compare the diagonal elements

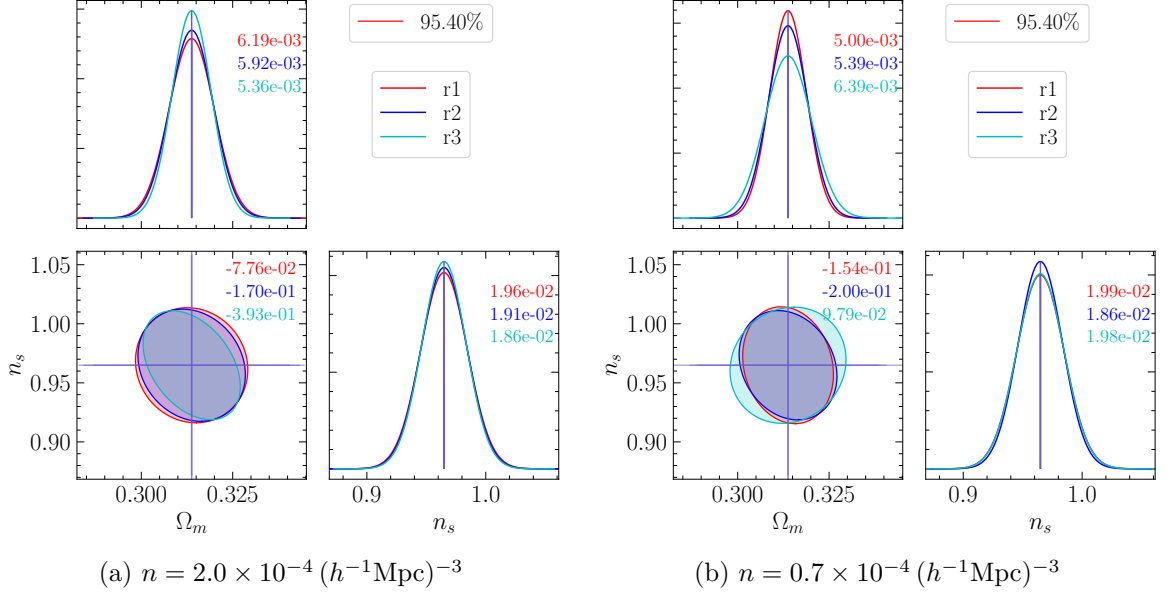


Figure 5: Corner plots from Fisher analysis performed using the optimized percentiles for the two tracer samples, for Ω_m , n_s . The ellipses show 95.4% confidence regions. The three colours correspond to three simulation realizations, and the widths(σ) of the marginalized 1D distribution are quoted in corresponding colours along with the 1D distributions. The correlation coefficients are quoted alongside the 2D ellipses. It is seen that the results are quite stable, with constraints $\lesssim 2\%$ on both the parameters.

of the jackknife covariance matrix with those computed from the full ensemble of simulation realizations. Figure 7 shows this ratio for both tracer samples. The comparison indicates that the jackknife estimates are not reliable in an absolute sense and must be rescaled to provide more accurate error estimates. We adopt the following scaling prescription:

$$C_{ij,jk}^{\text{scaled}} = C_{ij,jk} \sqrt{\frac{C_{ii}C_{jj}}{C_{ii,jk}C_{jj,jk}}}, \quad (4.1)$$

which sets the diagonal errors of the jackknife matrix to those of the full covariance, while preserving its correlation structure. While we do not currently offer a method to determine this scaling in the absence of the full simulation ensemble, we aim to improve the jackknife covariance estimate using existing methods (see, e.g., [35, 36]) and explore other solutions for this in future work, possibly using semi-analytical techniques.

Once the covariance matrices are appropriately scaled, we follow the procedure described in Section 3.2 to compute the X^s , Y^s , and Z^s statistics for both tracer samples and both cosmological parameters. Figure 8 shows the scatter plots of X^s versus Y^s , with points colored by their corresponding Z^s values. A single line is drawn in all four panels to approximately separate regions of low and high Z^s . Data points that lie below this line for both cosmological parameters and satisfy $Z^s \leq Z_{\text{th}}$ are selected as valid for each tracer sample. We find that the results are largely insensitive to the specific choice of Z_{th} (here set to 3), and the defining constraint is primarily the line in the X^s - Y^s plane. After identifying the valid points, we perform the full minimization procedure described in Section 3.2 to select the optimal subset based on the stability of the 1D marginalized errors.

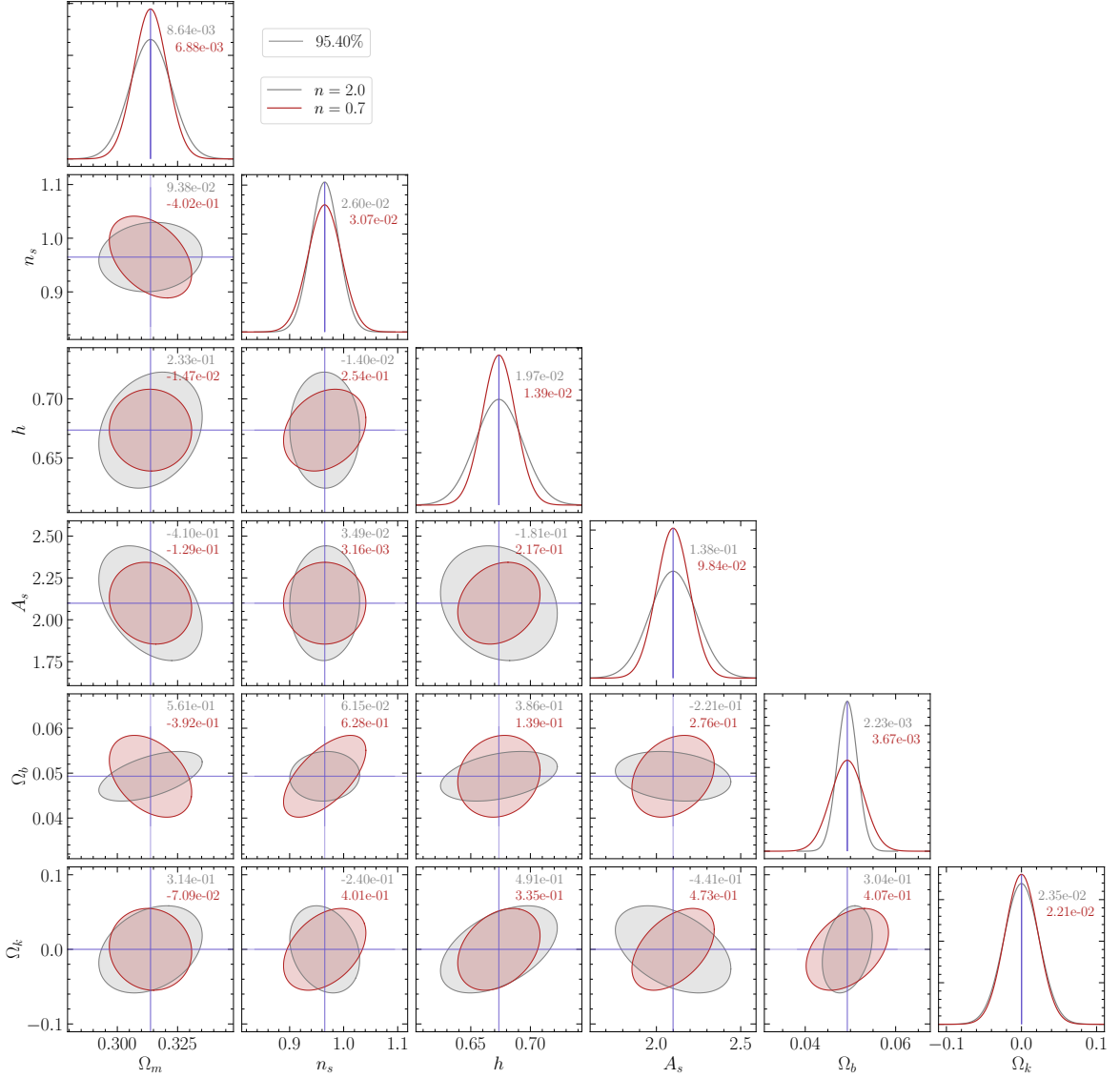


Figure 6: Corner plots from Fisher analysis performed using the same percentiles as in Figure 5, but for constraining all the 6 cosmological parameters. Grey (red) colour corresponds to the higher (lower) number density tracer sample. The number densities n are quoted in units of $10^{-4}(h^{-1}\text{Mpc})^{-3}$.

Finally, we perform the Fisher analysis and present the results in Figure 9. The grey contours represent forecasts from 10 randomly chosen jackknife realizations. The colored contours show results from the three simulation realizations, using the true covariance matrices and accurate slopes, but applying the same optimized set of VVF percentiles. In particular, the red contour corresponds to the same realization (r1) as one of the jackknife runs, allowing direct comparison. We observe reasonable agreement between the red and grey contours in terms of the degeneracy direction. However, the jackknife estimates tend to overestimate the marginalized errors by up to $\sim 30\%$ in some cases, likely due to residual inaccuracies in the jackknife covariance matrix. Additionally, jackknife resampling does not fully capture the

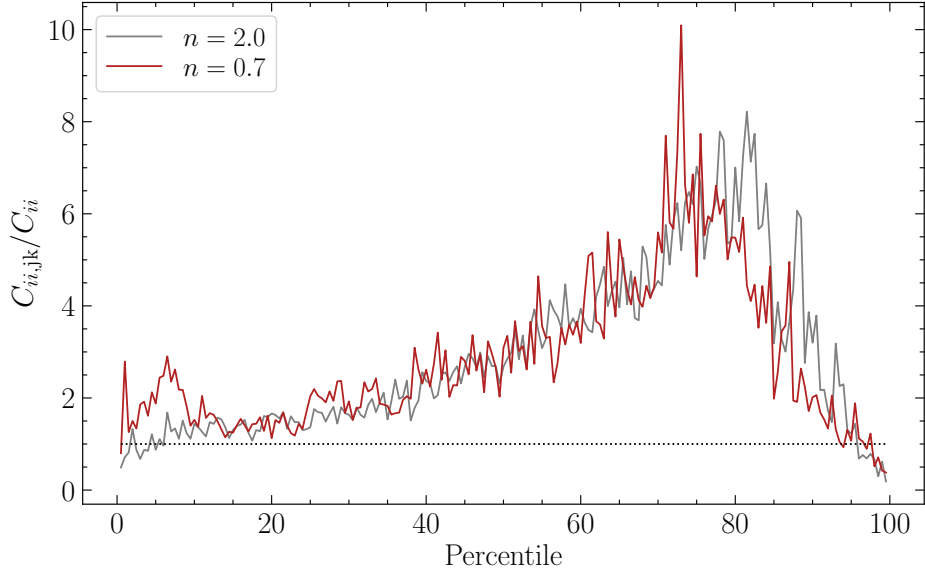


Figure 7: Ratios of the diagonal errors from jackknife covariance to those from the true covariance for the two number densities. The dotted line represents the ratio equal to 1 (unbiased diagonal errors). It is seen that jackknife over-estimates the errors for most of the lower percentiles, and under-estimates it for the highest percentiles. See 4.2 for details.

variations across different simulation seeds — the colored contours from the three simulations show significantly more scatter than the grey jackknife contours alone. Despite these limitations, the use of optimized data subsets leads to visibly more stable forecasts compared to the results obtained using fixed percentiles (see the *top right panel* of Figure 2). More importantly, the optimized approach yields up to a factor of 2 tighter constraints than those obtained using the full VVF and the fixed-percentile selection (*top left panel* of Figure 2), highlighting its effectiveness in selecting the most informative data points.

5 Discussion

Fisher forecasts are a standard tool for quantifying the information content of cosmological summary statistics. However, their reliability can be compromised when derivative estimates are noisy because the number of realizations is limited, as is often the case in simulation-based studies. In such scenarios, using randomly chosen data points can lead to unstable constraints. In this work, we presented a formalism to identify informative and stable subsets of summaries of halo-based statistics, which maximize the stability and information content in the Fisher forecast using these statistics. We illustrated the use of this formalism with the Voronoi volume function (VVF, [16]). Our method is motivated by practical limitations encountered in simulation-based cosmology, where both the number of realizations and the availability of cosmological variations are often constrained. Through this work, we offer a framework that remains effective across both well-sampled and data-limited regimes.

The formalism involves a two-step approach: averaging the statistic across multiple random sub-samples of the tracer population, followed by an optimization over subsets of summary statistic values (e.g., VVF percentiles). Random sub-sampling plays an important role in suppressing noise, while the subsequent optimization ensures that the selected data

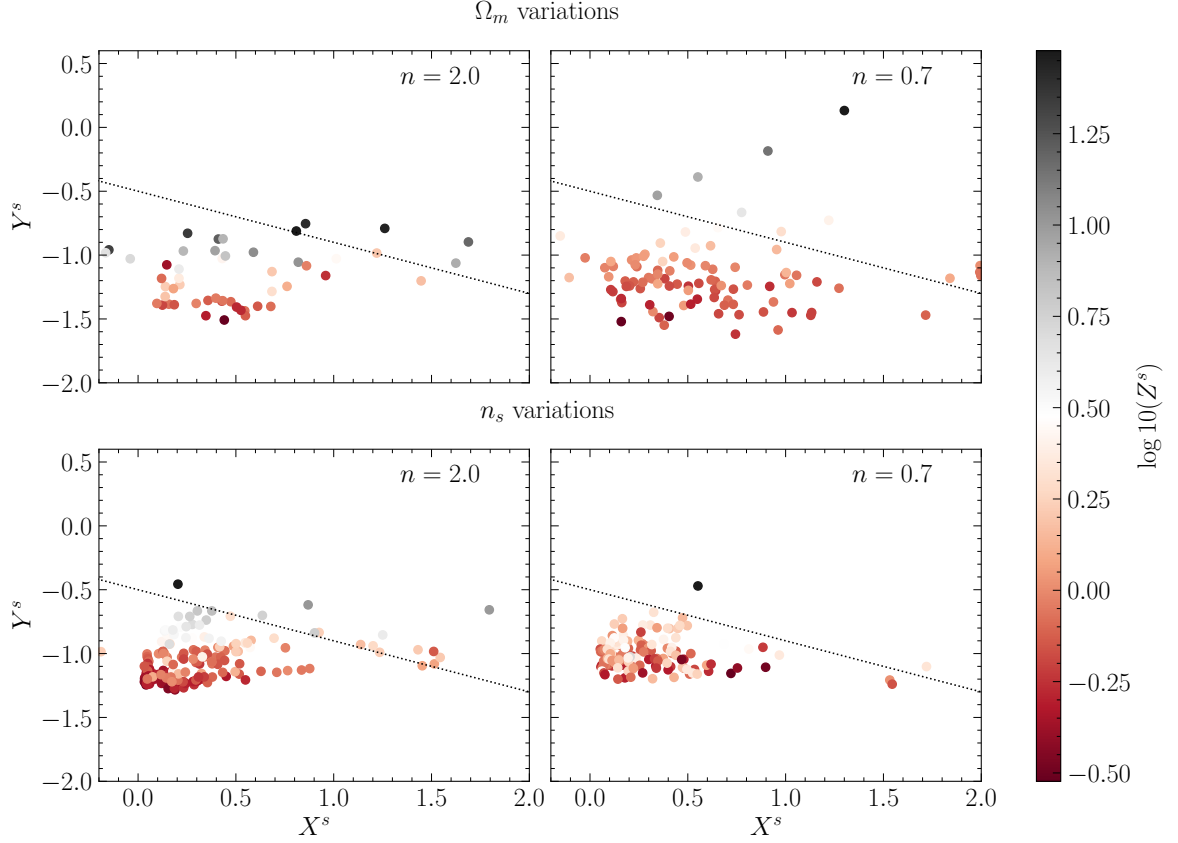


Figure 8: Similar to Figure 3 showing X_s, Y_s for the single realization optimization; with the points being coloured by their Z^s values, Z_{th} corresponding to white colour. See Section 4.2 for details.

points contribute maximal information in a stable manner. The combination leads to tighter and more consistent parameter constraints compared to fixed, heuristic choices.

In the case of the low-resolution **Sinhagad** simulation suite, we had access to multiple realizations per cosmology, allowing us to estimate the covariance matrix robustly and compute an accurate reference slope. This enabled the definition of three metrics— X , Y , and Z —to capture the accuracy, informativeness, and stability of derivative estimates. Using these diagnostics, we select an optimized subset of points that yield consistent and strong constraints. This is illustrated using the VVF to constrain the cosmological parameters Ω_m and n_s . Our analysis shows that these optimized subsets lead to comparatively stable Fisher forecasts compared to those obtained using un-optimized data points, with 1D marginalized uncertainties varying by $\leq 15\%$ ($\leq 30\%$) across realizations for the higher (lower) number density tracer sample considered. The constraints themselves are promising, with forecasted errors on Ω_m and n_s at the level of 2% or better, which are expected to improve with availability of higher resolution simulations. Although the absolute values of the constraints are not to be over-interpreted, we focus on the fact that random sub-sampling along with optimization can tighten the constraints by upto 50%.

In contrast, the high-resolution **Sahyadri** suite represents a more challenging setting where only a single realization is available per cosmology. To mimic this situation, we adapted

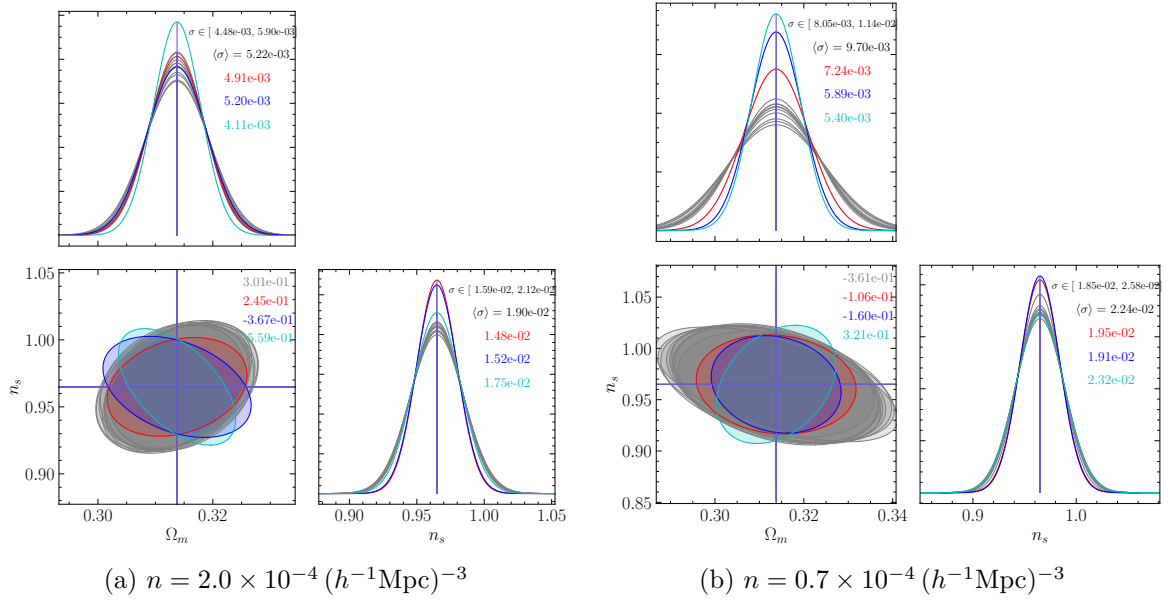


Figure 9: Corner plots from Fisher analysis performed using percentiles optimized with a single simulation realization. The plots are similar to Figure 5, with grey colour showing constraints from 10 randomly chosen jackknife realizations. The mean and range of σ in the 100 jackknife realizations, and the correlation coefficient of one randomly chosen jackknife realization are also reported. See Section 4.2 for details.

our formalism to operate using jackknife-based estimators, redefining $X \rightarrow X^s$, $Y \rightarrow Y^s$, and $Z \rightarrow Z^s$ accordingly. Our selection procedure, although less robust, continued to identify percentile subsets that yield relatively stable and tighter forecasts. A notable challenge in the single realization setting was the inaccuracy of jackknife covariance estimates. To fix this, we introduced a simple scaling procedure to align jackknife-derived covariances with those obtained from full simulation ensembles. While this scaling relies on empirical calibration using the true covariance (which may not be readily available), it significantly improved the agreement of Fisher constraints and is a promising direction for further development, possibly using semi-analytical techniques.

Although this work has focused on the VVF, the proposed method is general and can be applied to any summary statistic where derivative estimates are noisy. In practical analyses involving cosmological simulations or observational data, computational limitations and sparse sampling are common challenges. E.g., currently popular machine learning techniques such as SBI applications often require $\mathcal{O}(100)$ realizations for robust derivative estimation, which might not always be feasible. Our formalism remains effective under such constraints and improves the reliability of parameter forecasts even with limited inputs.

Future work will focus on extending this framework in several directions. One priority is to develop a systematic approach for modifying jackknife covariance estimates in the absence of reference covariance matrices. We also plan to apply this methodology to higher-resolution simulations within the full **Sahyadri** suite, where denser tracer populations should allow for more precise and stable constraints. In addition, the method will be tested on combinations of multiple summary statistics – such as the VVF and the two point correlation function – to evaluate potential gains in parameter sensitivity. These improvements will allow for

thorough testing of the method’s effectiveness and applicability in real-world cosmological applications.

Data availability

Acknowledgments

We gratefully acknowledge the participants of the Pune-Mumbai Cosmology & Astro-Particle (PMCAP) series of meetings (https://www.tifr.res.in/~shadab.alam/PM_CAP_meeting/) for stimulating discussions that inspired the construction of the simulations used in this work. We are especially grateful to Arka Banerjee for originally pointing out that halo-based statistics are prone to strong biases due to noisy derivatives. The research of AP is supported by the Associates Scheme of ICTP, Trieste. This work made extensive use of the open source computing packages NumPy [37],³ SciPy [38],⁴ Pandas [39, 40],⁵ Matplotlib [41],⁶ and Jupyter Notebook.⁷ The analysis was performed on the Pegasus cluster at IUCAA, Pune.⁸

References

- [1] DESI Collaboration, A. Aghamousa, J. Aguilar, S. Ahlen, S. Alam, L.E. Allen et al., *The DESI Experiment Part I: Science, Targeting, and Survey Design*, *arXiv e-prints* (2016) [arXiv:1611.00036](#) [[1611.00036](#)].
- [2] DESI Collaboration, M. Abdul-Karim, J. Aguilar, S. Ahlen, S. Alam, L. Allen et al., *DESI DR2 Results II: Measurements of Baryon Acoustic Oscillations and Cosmological Constraints*, *arXiv e-prints* (2025) [arXiv:2503.14738](#) [[2503.14738](#)].
- [3] Ž. Ivezić, S.M. Kahn, J.A. Tyson, B. Abel, E. Acosta, R. Allsman et al., *LSST: From Science Drivers to Reference Design and Anticipated Data Products*, *ApJ* **873** (2019) 111 [[0805.2366](#)].
- [4] R. Laureijs, J. Amiaux, S. Arduini, J.L. Auguères, J. Brinchmann, R. Cole et al., *Euclid Definition Study Report*, *arXiv e-prints* (2011) [arXiv:1110.3193](#) [[1110.3193](#)].
- [5] A. Banerjee and T. Abel, *Nearest neighbour distributions: New statistical measures for cosmological clustering*, *MNRAS* **500** (2021) 5479 [[2007.13342](#)].
- [6] A. Banerjee and T. Abel, *Cosmological cross-correlations and nearest neighbour distributions*, *MNRAS* **504** (2021) 2911 [[2102.01184](#)].
- [7] R.K. Sheth and G. Tormen, *On the environmental dependence of halo formation*, *MNRAS* **350** (2004) 1385 [[astro-ph/0402237](#)].
- [8] M. White, *A marked correlation function for constraining modified gravity models*, *J. Cosmology Astropart. Phys.* **2016** (2016) 057 [[1609.08632](#)].
- [9] J. Schmalzing and T. Buchert, *Beyond Genus Statistics: A Unifying Approach to the Morphology of Cosmic Structure*, *ApJ* **482** (1997) L1 [[astro-ph/9702130](#)].
- [10] C. Hikage, J. Schmalzing, T. Buchert, Y. Suto, I. Kayo, A. Taruya et al., *Minkowski Functionals of SDSS Galaxies I : Analysis of Excursion Sets*, *PASJ* **55** (2003) 911 [[astro-ph/0304455](#)].

³<http://www.numpy.org>

⁴<http://www.scipy.org>

⁵<https://pandas.pydata.org>

⁶<https://matplotlib.org/>

⁷<https://jupyter.org>

⁸<http://hpc.iucaa.in>

- [11] J. Alsing and B. Wandelt, *Generalized massive optimal data compression*, [*MNRAS* **476** \(2018\) L60](#) [[1712.00012](#)].
- [12] T. Charnock, G. Lavaux and B.D. Wandelt, *Automatic physical inference with information maximizing neural networks*, [*Phys. Rev. D* **97** \(2018\) 083004](#) [[1802.03537](#)].
- [13] P. Lemos, M. Cranmer, M. Abidi, C. Hahn, M. Eickenberg, E. Massara et al., *Robust simulation-based inference in cosmology with Bayesian neural networks*, [*Machine Learning: Science and Technology* **4** \(2023\) 01LT01](#) [[2207.08435](#)].
- [14] P. Lemos, L. Parker, C. Hahn, S. Ho, M. Eickenberg, J. Hou et al., *Field-level simulation-based inference of galaxy clustering with convolutional neural networks*, [*Phys. Rev. D* **109** \(2024\) 083536](#).
- [15] B. Semelin, R. Mériot, A. Mishra and D. Cornu, *Combining summary statistics with simulation-based inference for the 21 cm signal from the Epoch of Reionisation*, [*A&A* **698** \(2025\) A35](#) [[2411.14419](#)].
- [16] A. Paranjape and S. Alam, *Voronoi volume function: a new probe of cosmology and galaxy evolution*, [*MNRAS* **495** \(2020\) 3233](#) [[2001.08760](#)].
- [17] S. Alam, A. Paranjape and J.A. Peacock, *Impact of tidal environment on galaxy clustering in GAMA*, [*MNRAS* **527** \(2024\) 3771](#) [[2305.01266](#)].
- [18] C. Hahn, F. Villaescusa-Navarro, E. Castorina and R. Scoccimarro, *Constraining M_V with the bispectrum. Part I. Breaking parameter degeneracies*, [*J. Cosmology Astropart. Phys.* **2020** \(2020\) 040](#) [[1909.11107](#)].
- [19] A. Banerjee, N. Kokron and T. Abel, *Modelling nearest neighbour distributions of biased tracers using hybrid effective field theory*, [*MNRAS* **511** \(2022\) 2765](#) [[2107.10287](#)].
- [20] J. Alsing, T. Charnock, S. Feeney and B. Wandelt, *Fast likelihood-free cosmology with neural density estimators and active learning*, [*MNRAS* **488** \(2019\) 4440](#) [[1903.00007](#)].
- [21] T.L. Makinen, T. Charnock, P. Lemos, N. Porqueres, A.F. Heavens and B.D. Wandelt, *The Cosmic Graph: Optimal Information Extraction from Large-Scale Structure using Catalogues*, [*The Open Journal of Astrophysics* **5** \(2022\) 18](#) [[2207.05202](#)].
- [22] Planck Collaboration, N. Aghanim, Y. Akrami, M. Ashdown, J. Aumont, C. Baccigalupi et al., *Planck 2018 results. VI. Cosmological parameters*, [*A&A* **641** \(2020\) A6](#) [[1807.06209](#)].
- [23] V. Springel, R. Pakmor, O. Zier and M. Reinecke, *Simulating cosmic structure formation with the GADGET-4 code*, [*MNRAS* **506** \(2021\) 2871](#) [[2010.03567](#)].
- [24] R. Scoccimarro, *Transients from initial conditions: a perturbative analysis*, [*MNRAS* **299** \(1998\) 1097](#) [[astro-ph/9711187](#)].
- [25] P.S. Behroozi, R.H. Wechsler and H.-Y. Wu, *The ROCKSTAR Phase-space Temporal Halo Finder and the Velocity Offsets of Cluster Cores*, [*ApJ* **762** \(2013\) 109](#) [[1110.4372](#)].
- [26] P.S. Behroozi, R.H. Wechsler, H.-Y. Wu, M.T. Busha, A.A. Klypin and J.R. Primack, *Gravitationally Consistent Halo Catalogs and Merger Trees for Precision Cosmology*, [*ApJ* **763** \(2013\) 18](#) [[1110.4370](#)].
- [27] J. Carretero, F.J. Castander, E. Gaztañaga, M. Crocce and P. Fosalba, *An algorithm to build mock galaxy catalogues using MICE simulations*, [*MNRAS* **447** \(2015\) 646](#) [[1411.3286](#)].
- [28] J. Chaves-Montero, R.E. Angulo, J. Schaye, M. Schaller, R.A. Crain, M. Furlong et al., *Subhalo abundance matching and assembly bias in the EAGLE simulation*, [*MNRAS* **460** \(2016\) 3100](#) [[1507.01948](#)].
- [29] J. DeRose, M.R. Becker and R.H. Wechsler, *Modeling Redshift-space Clustering with Abundance Matching*, [*ApJ* **940** \(2022\) 13](#) [[2105.12104](#)].

- [30] P. Bett, V. Eke, C.S. Frenk, A. Jenkins, J. Helly and J. Navarro, *The spin and shape of dark matter haloes in the Millennium simulation of a Λ cold dark matter universe*, [MNRAS **376** \(2007\) 215](#) [[astro-ph/0608607](#)].
- [31] G. Voronoi, *Nouvelles applications des paramètres continus à la théorie des formes quadratiques. deuxième mémoire. recherches sur les paralléloèdres primitifs.*, *Journal für die reine und angewandte Mathematik* **134** (1908) 198.
- [32] S.P. Driver, D.T. Hill, L.S. Kelvin, A.S.G. Robotham, J. Liske, P. Norberg et al., *Galaxy and Mass Assembly (GAMA): survey diagnostics and core data release*, [MNRAS **413** \(2011\) 971](#) [[1009.0614](#)].
- [33] S.P. Driver, S. Bellstedt, A.S.G. Robotham, I.K. Baldry, L.J. Davies, J. Liske et al., *Galaxy And Mass Assembly (GAMA): Data Release 4 and the $z \in [0.1, 0.15]$ total and $z \in [0.08, 0.15]$ morphological galaxy stellar mass functions*, [MNRAS **513** \(2022\) 439](#) [[2203.08539](#)].
- [34] A.F. Heavens, R. Jimenez and O. Lahav, *Massive lossless data compression and multiple parameter estimation from galaxy spectra*, [MNRAS **317** \(2000\) 965](#) [[astro-ph/9911102](#)].
- [35] B. Efron and C. Stein, *The jackknife estimate of variance*, *The Annals of Statistics* **9** (1981) 586.
- [36] Euclid Collaboration, K. Naidoo, J. Ruiz-Zapatero, N. Tessore, B. Joachimi, A. Loureiro et al., *Euclid preparation. Accurate and precise data-driven angular power spectrum covariances*, [arXiv e-prints \(2025\) arXiv:2506.09118](#) [[2506.09118](#)].
- [37] S. Van Der Walt, S.C. Colbert and G. Varoquaux, *The NumPy array: a structure for efficient numerical computation*, *ArXiv e-prints* (2011) [[1102.1523](#)].
- [38] P. Virtanen, R. Gommers, T.E. Oliphant, M. Haberland, T. Reddy, D. Cournapeau et al., *SciPy 1.0: Fundamental Algorithms for Scientific Computing in Python*, [Nature Methods **17** \(2020\) 261](#).
- [39] Wes McKinney, *Data Structures for Statistical Computing in Python*, in *Proceedings of the 9th Python in Science Conference*, Stéfan van der Walt and Jarrod Millman, eds., pp. 56 – 61, 2010, [DOI](#).
- [40] T. pandas development team, *pandas-dev/pandas: Pandas*, Feb., 2020. 10.5281/zenodo.3509134.
- [41] J.D. Hunter, *Matplotlib: A 2d graphics environment*, [Computing In Science & Engineering **9** \(2007\) 90](#).
- [42] M. Tegmark, A.N. Taylor and A.F. Heavens, *Karhunen-Loève Eigenvalue Problems in Cosmology: How Should We Tackle Large Data Sets?*, [ApJ **480** \(1997\) 22](#) [[astro-ph/9603021](#)].

A Covariance and Fisher matrices

The covariance matrices used in the main text are estimated using two approaches: one based on 100 independent default realizations, and the other based on a single realization. For the multiple realization method, the covariance is computed using the standard formula from the VVFs of 100 realizations, excluding $r1$:

$$C_{ij} = \frac{1}{N-1} \sum_{k=2}^{N+1} (y_i^k - \langle y_i \rangle)(y_j^k - \langle y_j \rangle). \quad (\text{A.1})$$

Here, y_i^k is the value of the VVF at i -th percentile, for the k -th realization, $\langle y_i \rangle \equiv \sum_{k=2}^{N+1} y_i^k$, and $N = 100$ in our case.

In the single-realization approach, 100 jackknife samples are generated by subdividing the simulation box into 10×10 cuboids along the x and y axes, resulting in 100 subvolumes. For each jackknife sample, one cuboid is masked, and the VVF is computed from the remaining volume. These 100 jackknife realizations are used to estimate the covariance matrix using the following equation:

$$C_{ij,jk} = \frac{N_{jk}-1}{N_{jk}} \sum_{k=1}^{N_{jk}} (y_i^k - \langle y_i \rangle_{jk})(y_j^k - \langle y_j \rangle_{jk}), \quad (\text{A.2})$$

where $N_{jk} = 100$ is the number of jackknife realizations, y_i^k is the value of the VVF at i th percentile for the k th jackknife realization, and the averages are taken across all N_{jk} realizations. As is shown in section 4.2, this method does not yield an unbiased estimate of the true covariance and requires scaling to produce reliable Fisher forecasts.

The derivatives with respect to the cosmological parameters are estimated using the three-point central difference method across seed-matched simulations:

$$\tilde{y}_{,\alpha} \equiv \frac{\partial \tilde{y}}{\partial \theta_\alpha} = \frac{\tilde{y}(\theta_{0\alpha} + \Delta\theta_\alpha) - \tilde{y}(\theta_{0\alpha} - \Delta\theta_\alpha)}{2\Delta\theta_\alpha} \quad (\text{A.3})$$

where the data vectors \tilde{y} are calculated from the $\pm\Delta$ variations of the α th cosmological parameter, whose fiducial value is θ_{0j} .

While performing the Fisher analysis, we make the following assumptions: (a) the likelihood is Gaussian, and (b) the data covariance matrix C_{ij} is independent of the cosmological parameters θ_α within the $\Delta\theta$ variations considered here. Then, the Fisher matrix simplifies to [42]:

$$F_{\alpha\beta} = \frac{\partial \tilde{y}}{\partial \theta_\alpha} C^{-1} \frac{\partial \tilde{y}}{\partial \theta_\beta}. \quad (\text{A.4})$$

The inverse Fisher matrix F_{ij}^{-1} corresponds to the posterior covariance matrix of the cosmological parameters under the assumption of very broad priors.

B Random sub-sampled vs Full VVF

Here, we compare the quality of the VVF estimated using the full sample versus the random sub-sampled version, with the aim of determining which approach is more suitable for performing Fisher forecasts. To make this comparison, we apply the analysis described in Section 3.1, selecting valid data points based on the metrics X, Y, Z defined earlier.

Figure 10 displays the cuts on X, Y, Z for both estimation methods. Data points failing the threshold $Z \leq Z_{\text{th}}$ are marked with open symbols and rejected. Visually, it is seen that the full VVF yields higher values of X, Y, Z , leading to a smaller fraction of the points being considered valid. Table 3 summarizes the number of valid points retained for each tracer sample under both methods. It is seen that the random sub-sampled VVF consistently results in a greater number of valid data points. This indicates that random sub-sampling improves the stability of the derivative estimates and provides a broader pool of usable points for Fisher analysis. We therefore adopt the random sub-sampled VVF as the default estimator in our study.

Random sub-sampling	Variation	Number of valid points	
		$n = 2.0$	$n = 0.7$
True	Δ	81	88
False	Δ	65	31
True	$\Delta/2$	34	56
False	$\Delta/2$	16	11

Table 3: Number of valid points available for different data sets.

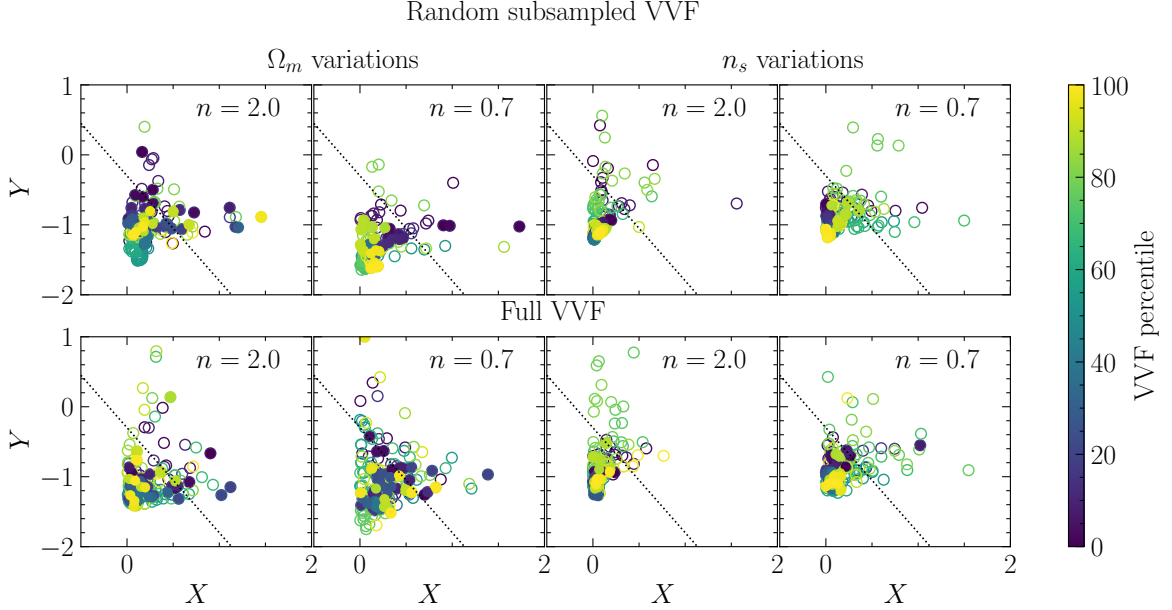


Figure 10: Comparison between the full VVF and the random sub-sampled VVF. The panels are the same as in Figure 3. The top (bottom) panel corresponds to the random sub-sampled (full) VVF. The number densities n are quoted in units of $10^{-4}(h^{-1}\text{Mpc})^{-3}$. Both are for $\pm\Delta$ variations of the cosmological parameters.

C Choice of parameter variations

In many practical settings, the computational cost of running high-resolution simulations limits the number of cosmological parameter variations that can be explored. This constraint applies to our under-construction **Sahyadri** simulation suite, where we restrict ourselves to $\pm\Delta$ variations around the fiducial values for each cosmological parameter. On the other hand, the lower-resolution simulations in the **Sinhagad** suite are computationally inexpensive, making them ideal for testing different variation schemes and assessing their impact on the stability and constraining power of derivative estimates. We use this flexibility to compare the performance of two choices: $\pm\Delta/2$ and $\pm\Delta$, where Δ corresponds to the default parameter step size adopted in this paper.

In this paper, derivatives are computed using a three-point central difference method. Choosing Δ to be too large risks violating the assumption of local linearity in the statistic-parameter relation. Conversely, too small a variation increases the noise arising from stochastic effects such as halo finder fluctuations, resulting in highly unstable derivative es-

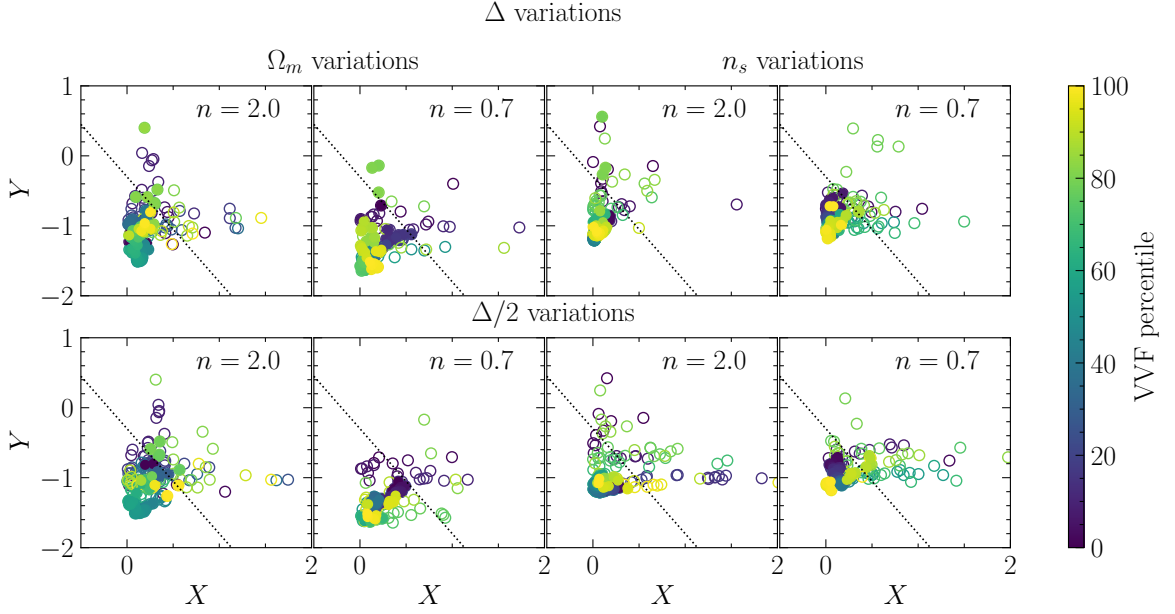


Figure 11: Comparison between the variation of cosmological parameters. The panels are same as Figure 10, except here the top (bottom) row corresponds to $\pm\Delta$ ($\pm\Delta/2$) variations. The random sub-sampled VVF is used in both the cases. It is visually apparent that more valid points are available in the $\pm\Delta$ case.

timates.

Following the same procedure as in Appendix B, we evaluate the metrics X, Y, Z for both variation schemes. As shown in Figure 11, the Δ variation leads to lower (and more favorable) values of these diagnostics, resulting in a larger number of points being accepted as valid. This trend is also confirmed by the summary in Table 3. Based on these results, we adopt the $\pm\Delta$ variation scheme for the remainder of this paper.